Volume 9 | Number 10 | 21 May 2025

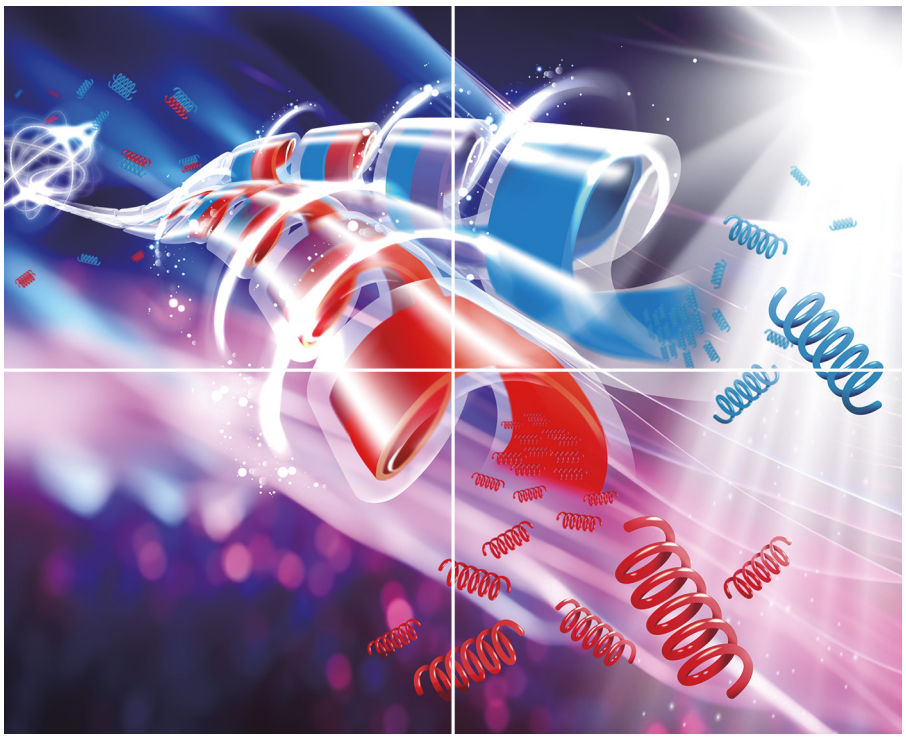

MATERIALS CHEMISTRY

FRONTIERS

CCS 中国化学会 CHINESE CHEMICAL SOCIETY

ICCAS 1956

ROYAL SOCIETY OF CHEMISTRY

rsc.li/frontiers-materials

MATERIALS CHEMISTRY FRONTIERS

RESEARCH ARTICLE

View Article Online
View Journal | View Issue

Cite this: *Mater. Chem. Front.*, 2025, **9**, 1501

Chirality expression from hierarchical foldamer-mesoscopic helical silica frameworks†

Piyanan Pranee,[ac] Robin Hess,[a] Anthony Boudier,[ab] Zakaria Anfar,[a] Matheus De Souza Lima Mendes,[a] Eric Merlet,[a] Wijak Yospanya,[c] Emilie Pouget,[a] Sylvain Nlate,[a] Céline Olivier,[b] Thierry Buffeteau,[b] Yann Ferrand*[a] and Reiko Oda*[ac]

Received 29th December 2024,
Accepted 24th March 2025

DOI: 10.1039/d4qm01140f

rsc.li/frontiers-materials

The interaction between racemic quinoline-derived helical oligoamide foldamers and mesoscopic silica-based helical frameworks was investigated. These foldamers displayed distinct chiroptical properties such as electronic and vibrational circular dichroism (ECD and VCD, respectively) and circularly polarized luminescence (CPL) when interacting with silica nanohelices (INHs) deposited as thin films. Dissymmetry factors (g_{abs} and g_{lum}) were influenced by drying kinetics, silica surface functional groups, and foldamer concentration and length. Washing co-assembled films of quinoline octamers and INHs in order to separate the two, revealed that ECD signals originated from molecular solution of foldamers which decreased over 7 minutes, indicating enantiomeric enrichment even though modest (~4%) induced by INHs. The induced foldamer handedness matched with the helicity of the INHs. Enantiopure foldamers (helically locked *M* or *P* oligomers) exhibited enhanced or reduced ECD signals depending on their helicity alignment with INHs. This study highlights the interplay between molecular chirality and supramolecular organization of foldamers directed by silica nanohelices.

1. Introduction

By its very nature, chirality is a hierarchical and multi-scale phenomenon. The recognition, induction, and transfer of chiral information between objects have garnered significant attention in the scientific community due to their strong implications in asymmetric catalysis, enantioselective reactions, and separation processes.[1,2] While extensive studies have focused on chirality induction between small molecules or macromolecules of similar size, many questions remain unanswered about the mechanisms of chiral information transmission between objects of vastly different scales, particularly between molecular chirality and purely morphological, much larger-scale chiral structures. In this context, the design and synthesis of chiral materials across diverse types and sizes have been a continuous pursuit.[3–5] Recently, advances have been made in the development of mesoscopic chiral inorganic materials, ranging from tens of nanometers to micrometers[6,7] often exhibiting enhanced optical activity due to their highly tunable morphologies.[7,8] The use of different soft-templating assembly methods has enabled the preparation of materials with controlled chiral morphologies.[9,10] Even if their constituent components are achiral, morphologically chiral structures at the mesoscopic level can still exhibit chiral properties across different fields. Understanding and controlling the chiral properties of these structures is essential for designing advanced materials and developing new technologies. We have developed helical nanostructures made of amorphous silica, devoid of any chiral molecules.[11–14] Using these mesoscopic inorganic structures as chiral platforms, we have highlighted the induction of chirality in otherwise achiral systems such as monoatomic anion,[15] chromophores,[16–18] gold nanoparticles,[19] carbon nanodots[20] and perovskite nanocrystals.[21–23]

Foldamers are synthetic oligomers that adopt folded conformations inspired by the structures of biopolymers. Aromatic oligoamides represent an interesting class of foldamers. The sequences composed of 8-amino-2-quinoline-carboxylic are shown in Fig. 1(a). Their exceptional helical conformational stability arises from intramolecular hydrogen bonds between the protons of the amide functions and the endocyclic nitrogen atoms of the adjacent aromatic rings. Furthermore, helical folding is assured by additional interactions within the helix such as electrostatic repulsions and conjugation (Fig. 1(b)).[24] Devoid of any stereogenic center, quinoline oligoamide foldamers

[a] *Institute of Chemistry & Biology of Membranes & Nano-objects (CBMN), University of Bordeaux, CNRS, Bordeaux INP, UMR 5248, F-33600 Pessac, France. E-mail: yann.ferrand@u-bordeaux.fr, reiko.oda@u-bordeaux.fr*
[b] *Institute of Molecular Sciences (ISM), University of Bordeaux, CNRS, Bordeaux INP, UMR 5255, F-33405 Talence, France*
[c] *WPI-Advanced Institute for Materials Research, Tohoku University, 2-1-1, Katahira, Aoba-Ku, Sendai 980-8577, Japan*

† Electronic supplementary information (ESI) available. See DOI: https://doi.org/10.1039/d4qm01140f

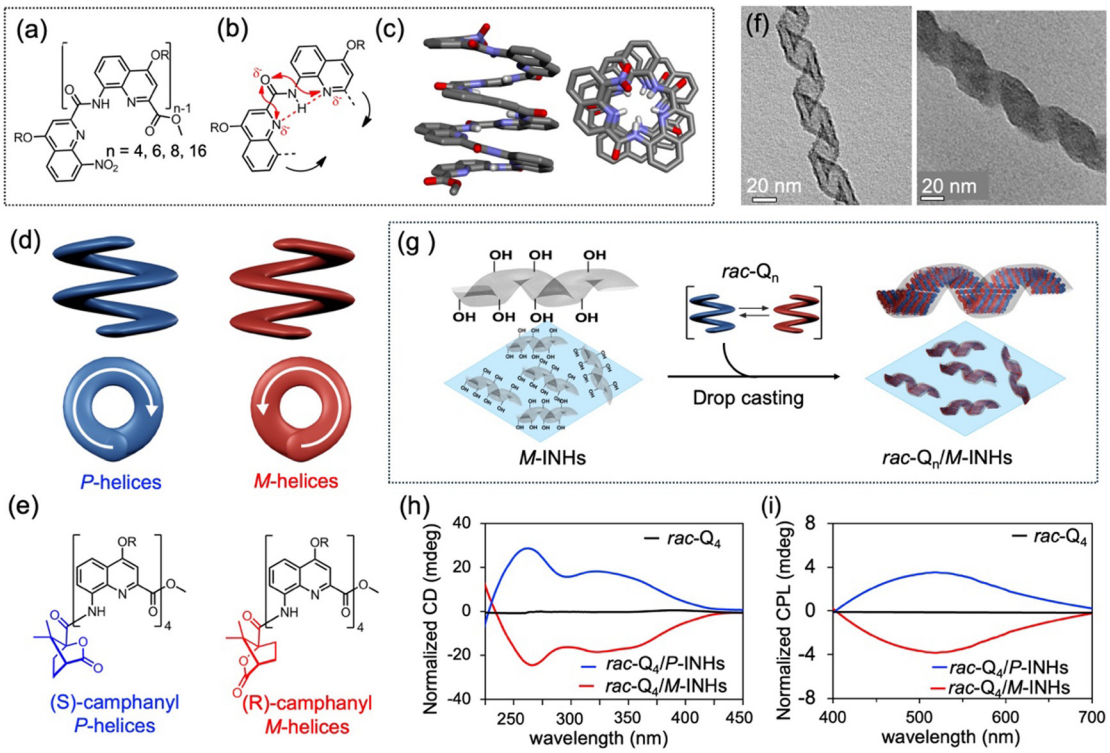

Fig. 1 (a) Chemical structures of a *rac*-Q$_n$ (n = 4, 6, 8, 16) sequences with a nitro group at the N-terminus. (b) Folding principles of *rac*-Q$_n$ oligomers; hydrogen bonds (···) are shown in red dotted lines whereas electrostatic repulsions (↔) are indicated with red arrows. (c) Side- and top-view of the X-ray structure of Q$_8$. Sidechains, hydrogens and solvent molecules are removed for clarity.[32,33] (d) Schematic representation of a *P*- and a *M*-handed helices. (e) Chemical structures of *P*-Q$_4$ (blue) and *M*-Q$_4$ (red). (f) TEM images of INHs before (left) and after (right) drop-casting *rac*-Q$_4$. (g) Illustration of the drop-casting approach of racemic oligoamide foldamers (*rac*-Q$_n$) with INHs. (h) Normalized ECD-absorption and (i) CPL spectra of *rac*-Q$_4$/INHs and *rac*-Q$_4$ after drop casting at 20 °C using toluene as a solvent.

exist as a dynamic mixture of left- and right-handed (*M*- and *P*-, respectively) helices (Fig. 1(c) and (d)). Yet, their helicity can be biased towards a single enantiomer when a chiral moiety is covalently attached at one end of the strand,[25–27] directly within the sequences[28] or when chiral molecules are confined within the helical cavities of the foldamers.[29] Their dynamic nature and modularity make them highly promising candidates for applications in chiral recognition, asymmetric catalysis, electro-optical devices,[30] and biomaterial-inspired applications.[31]

In this study, we investigate how small racemic aromatic helices and helically shaped mesoscopic inorganic silica nano-objects interact with each other, in order to elucidate how chiral structures of vastly different sizes can interact and subsequently transfer their chiral information.

2. Experimental

2.1 Preparation of inorganic silica nanohelices (Fig. 1(f))

The synthesis of gemini (16-2-16) tartrate surfactant was previously reported. Briefly, gemini cationic surfactant, *N*,*N*′-dihexadecyl-*N*,*N*,*N*′,*N*′-tetramethylethylene diammonium (abbreviated as 16-2-16) having chiral L- or D-tartrate counterions was solubilized in water (1.0 mM) by heating the solution at 70 °C for 5 min, sonicated for 3 min at room temperature, and heating again at 70 °C for 5 min before aging at 20 °C for 4 days to form organic helical nanostructures. The handedness of the helices was determined by the enantiomer of tartrate: with L-tartrate, right-handed (*P*) helices were formed and with D-tartrate, left-handed (*M*) helices were obtained.[34] These chiral helical structures were then used as soft templates to prepare hybrid nanohelices *via* sol–gel polycondensation of tetraethyl orthosilicate (TEOS).[11,12] The pre-hydrolyzed TEOS was mixed with organic gel at 20 °C for 12 h. The precipitate was washed with cold water (3 times) to get rid of excess TEOS, resulting in organic–inorganic hybrid silica nanohelices (HNHs).

After preparing HNHs, the organic self-assembly of 16-2-16 L-/D-tartrate was subsequently removed by washing the HNHs with methanol at 70 °C (3 times) to obtain purely inorganic and amorphous silica nanohelices (INHs) with an empty chiral nanospace.[14] Finally, INHs were cut by tip sonication[13] and deposited on a substrate.

2.2 Preparation of amine-functionalized INHs (INHs-NH$_2$) and calcinated-INHs

To prepare INHs-NH$_2$, 10 μL of (3-aminopropyl)triethoxysilane (APTES) was added into 5 mL of INHs (1 mg mL^{-1}) suspension in ethanol, and sonicated for 10 min. Then, the suspension was stirred at 70 °C for 12 h. The excess APTES was removed by washing the suspension with ethanol (3 times). This process was repeated twice to assure the good grafting of APTES on the

surface of INHs. Calcinated-INHs was prepared by calcinating INHs at 600 °C for 2 h under air.

2.3 Synthesis of foldamers (*rac*-, *P*-, *M*-Q_n)

Racemic quinoline oligoamide helices (denoted hereafter as *rac*-Q_n with n = 4, 6, 8, and 16) were synthesized using 8-amino-2-quinoline-carboxylic acid as monomeric unit following a doubling segment strategy as previously reported (Fig. 1(a)).[32,35] Helically locked *M*-Q_4 and *P*-Q_4 were prepared by appending an enantiomerically pure camphanyl moiety (*R* or *S*, respectively) at the N-terminus of the helix (Fig. 1(e)).[25,27] Reactions were carried out under an inert atmosphere unless otherwise specified. Tetrahydrofurane (THF) and dichloromethane (CH_2Cl_2) were dried over alumina columns; chloroform ($CHCl_3$) was dried over oven dried potassium carbonate (K_2CO_3) then filtered and distilled from calcium hydride (CaH_2); triethylamine (NEt_3) and diisopropylethylamine (DIPEA) were distilled over calcium hydride (CaH_2). Reactions were monitored by thin layer chromatography on silica gel 60-F254 plates and observed under UV light. Column chromatography purifications were carried out on Si60 (40–63 μm).

2.4 Drop casting oligoamide foldamers (*rac*-Q_n)/chiral foldamers (*M*-Q_4 or *P*-Q_4) on INHs

A suspension of INHs (200 μg) in EtOH/iso-propanol (1 : 1) was deposited on a quartz substrate (2 × 2 cm^2) by using a drop-casting method, then dried. Then, 100 μL of 1.0 mM foldamer (*rac*-Q_n, *M*-Q_4 or *P*-Q_4) solution was drop-cast on the substrate, then dried at 20 °C for 24 h.

2.5 Study on solvent effect for drop-casting of *rac*-Q_4 on INHs

rac-Q_4 was prepared at 1.0 mM by using different solvents including benzene, toluene, chlorobenzene, *p*-chlorotoluene, aniline and nitrobenzene. Then, *rac*-Q_4 (1 mM, 100 μL) was drop-cast on a substrate (2 × 2 cm^2) containing INHs (200 μg) before drying at 20 °C for 24 h.

2.6 Kinetic study for enantiomeric enrichment of *rac*-Q_4 using INHs

rac-Q_4 was prepared at 1.0 mM by using different solvents including toluene, chlorobenzene and aniline. Then, *rac*-Q_4 (0.75 mM, 30 μL) was drop-cast on a substrate (2 × 2 cm^2) containing INHs (200 μg) before drying at 20 °C for 24 h.

2.7 Optimization of the ratio between *rac*-Q_4 and INHs

rac-Q_4 was prepared at different concentrations (0.25, 0.50, 0.75, and 1.0 mM) using toluene as a solvent. Then, 100 μL of *rac*-Q_4 solution was drop-cast on a quartz substrate (2 × 2 cm^2) containing 200 μg INHs and subsequently dried at 20 °C for 24 h.

2.8 Enantiomeric enrichment of *rac*-Q_n with different length

rac-Q_4, Q_6, Q_8 and Q_{16} were prepared at 1.0 mM using toluene or aniline as a solvent. Then, 100 μL of Q_4 solution was drop-cast on a quartz substrate (2 × 2 cm^2) containing 200 μg INHs and subsequently dried at 20 °C for 24 h.

2.9 Morphological analysis

The morphology of the silica nanohelices was characterized using transmission electron microscopy (TEM, CM120, Philips, Amsterdam, Netherlands). TEM observation samples were prepared by dropping 5 μL of silica nanohelices in ethanol/iso-propanol dispersion (0.05 μg μL^{-1}) onto a carbon supported copper grid and drying, without staining. The observation was performed at 120 kV.

2.10 Electronic circular dichroism (ECD) and UV-Vis measurements

ECD and UV-visible (UV-Vis) absorption spectra of the silica nanohelices and foldamer mixtures were recorded using a CD spectropolarimeter (J-815, JASCO Corp., Tokyo, Japan) equipped with a 1 mm path length quartz cell. Diffuse reflectance circular dichroism (DRCD) and UV-Vis spectra of the drop-cast films were obtained using an integrating sphere (DRCD-575) attached to the J-815.

2.11 Circularly polarized luminescence (CPL) and fluorescence measurements

CPL and fluorescence spectra of the drop-cast films were measured using a CPL spectrophotometer (CPL-300, JASCO Corp., Tokyo, Japan). The measurements were carried out with an HT voltage of 800–870 V. Emission was detected in the wavelength range of 400–700 nm. Samples were excited using monochromatic light with the wavelength of 320 nm.

2.12 Vibrational circular dichroism (VCD) measurement

Measurement of Q_4/INHs deposted on CaF_2 was performed using a ThermoNicolet Nexus 670 FTIR spectrometer equipped with a VCD optical bench. In this optical bench, the light beam was focused on the sample by a BaF_2 lens (191 mm focal length), passing an optical filter, a BaF_2 wire grid polarizer (Specac), and a ZnSe photoelastic modulator (Hinds Instruments, Type II/ZS50). The light was then focused by a ZnSe lens (38.1 mm focal length) onto a 1 × 1 mm^2 HgCdTe (ThermoNicolet, MCTA* E6032) detector. IR absorption and VCD spectra were recorded at a resolution of 4 cm^{-1}, by coadding 50 scans and 36 000 scans (12 h acquisition time), respectively. Since drop casting preparation may induce molecular orientation, the CaF_2 windows were placed on a rotating sample holder and the VCD spectra were obtained with the CaF_2 windows rotated at four angles around the light beam axis (0°, 45°, 90° and 135°). Raw VCD spectra of silica (*M*- and *P*-INHs) and foldamers (*rac*-Q_4/*M*-INHs, *rac*-Q_4/*P*-INHs, *P*-Q_4/*M*-INHs, *P*-Q_4/*P*-INHs, *M*-Q_4/*M*-INHs, *M*-Q_4/*M*-INHs, rac-Q_8/*M*-INHs and rac-Q_8/*P*-INHs) samples were obtained by averaging the four spectra. Baseline corrections of the raw VCD spectra of foldamer samples were performed by subtracting the raw VCD spectra of the silica samples. The photoelastic modulator was adjusted for maximum efficiency in the mid-IR region at 1400 cm^{-1}. Calculations were performed *via* the standard ThermoNicolet software, using Happ and Genzel apodization, de-Haseth phase-correction and a zero-filling factor of one.

3. Results and discussion

Foldamer/INHs co-assemblies were obtained by drop-casting solutions of racemic foldamers of varying length (*rac*-Q$_n$), onto either *P*- or *M*-INHs templates (Fig. 1(g)). More precisely, INHs (200 μg) dispersed in ethanol:iso-propanol mixture were deposited onto a 2 × 2 cm^2 quartz substrate and dried at room temperature for 1 h to form INHs thin films. Subsequently, a solution of racemic foldamers (*rac*-Q$_n$), prepared at a specific concentration in a suitable solvent, was drop-cast onto the INHs films, forming *rac*-Q$_n$/INHs films that were dried at a controlled temperature. It is important to note here that the chiral nanospace within the helices was previously calculated to be approximately 3 × 10^{-4} cm^3 mg^{-1} of nanohelices.[23] These helices are considerably larger than the molecular helices, with a helical pitch of ∼65 nm, and a diameter of ∼35 nm[14] compared to 0.35 nm and 2 nm respectively for a foldamer.

The chiroptical responses of *rac*-Q$_4$/INHs films (1 mM foldamer solution in toluene, drop-cast at 20 °C) were examined. They exhibited distinct symmetrical electronic circular dichroism (ECD) signals in the 230–450 nm range (Fig. 1(h) and Fig. S1a, ESI†) (negative or positive signals with *M*- or *P*-INHs, respectively) with dissymmetry factors g_{abs} at 324 nm of about 1.0 × 10^{-3}. Circularly polarized luminescent (CPL) signals were also observed upon excitation at 320 nm (Fig. 1(i) and Fig. S1b, ESI†), with g_{lum} around 1.0 × 10^{-3} at 505 nm. (see definition of g_{abs} and g_{lum} in Supplementary Information). The contribution from a Linear Dichroism (LD) effect was minimized by averaging the signals while rotating the sample at 0° and 90° (Fig. S2, ESI†).

The effect of solvent evaporation rate on the formation of *rac*-Q$_4$/INHs films was investigated at three temperatures: 4, 20, and 60 °C. The highest ECD and CPL signals were observed with slow toluene evaporation at 4 °C with g_{abs} ∼ ±1.5 × 10^{-3} and g_{lum} ∼ ±1.3 × 10^{-3}. These values decreased to g_{abs} ∼ ±1.0 × 10^{-4} and g_{lum} ∼ ±1.3 × 10^{-4} as the temperature increased to 60 °C (Fig. 2(a)–(d) and Fig. S3, ESI†).

The choice of solvents, characterized by their vapor pressure, boiling point (b.p.), and the solubility of the foldamers was also found to significantly influence the chiroptical responses. The g_{abs} and g_{lum} of *rac*-Q$_4$/INHs were evaluated in solvents with different b.p. (Fig. 2(e) and (f)) as summarized in Table S1 (ESI†) (1.0 mM solution, dried at 20 °C) and Fig. S4, S5 (ESI†). The results showed that higher dissymmetry factors were achieved with solvents that have intermediate b.p. values (110.8–184.4 °C) such as toluene, chlorobenzene, *p*-chlorotoluene or aniline yielding g_{abs} (∼±1.0 × 10^{-3}) and g_{lum} (∼±1.0 × 10^{-3}). In contrast, lower chiroptical properties were observed with solvents that have either lower or higher b.p., such as benzene (b.p. 80.3 °C) with g_{abs} ∼ ±1.5 × 10^{-4} and g_{lum} ∼ ±8.0 10^{-4}, or nitrobenzene (b.p. 211.1 °C) with g_{abs} ∼ ±4.0 × 10^{-4} and g_{lum} ∼ ±6.5 × 10^{-4}. For solvents yielding higher g_{abs}, such as toluene, chlorobenzene and aniline, the kinetics of chirality induction was monitored by measuring g_{abs} at regular intervals during the drying process at 20 °C. As shown in Fig. S6 (ESI†), toluene with the lowest b.p. was the fastest solvent to evaporate, the ECD signal induction occurred most rapidly, reaching a significant level in approximately 10 minutes. In contrast, with aniline, the drying occurred more slowly, and it took approximately 105 minutes for the ECD signal to reach the equilibrium. Meanwhile, the final values of induced ECD signals were of the same order among these solvents.

Finally, the foldamer concentration relative to the INHs film was evaluated and optimized. Various concentrations of Q$_4$ solutions (0.25–1.0 mM 100 μL, in toluene) were drop-cast onto

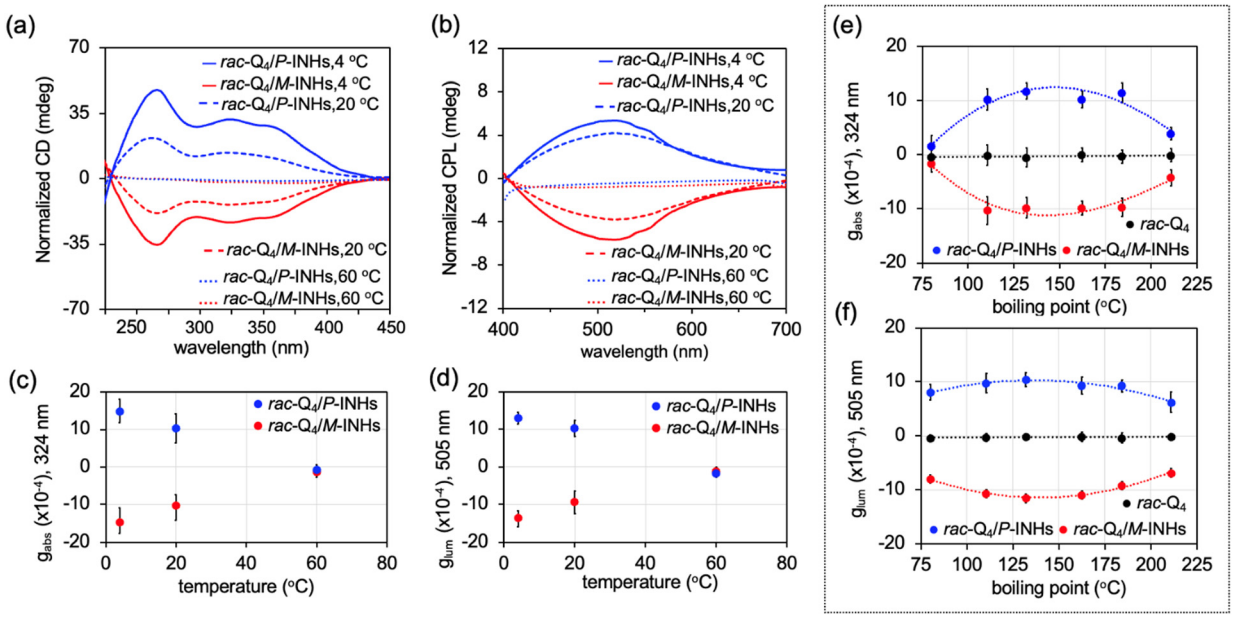

Fig. 2 (a) ECD-absorption spectra, (b) CPL spectra and (c) g_{abs} at 324 nm and (d) g_{lum} at 505 nm of *rac*-Q$_4$/INHs after drop-cast at different drying temperatures (4 °C, 20 °C and 60 °C) using toluene as a solvent. (e) g_{abs} and (f) g_{lum} of *rac*-Q$_4$/INHs drop-cast in solvents with different b.p. (°C).

the INHs substrate (200 μg, 20 °C). The highest g_{abs} ($\sim 2.0 \times 10^{-3}$) and g_{lum} ($\sim 1.7 \times 10^{-3}$) were observed at a concentration of 0.75 mM (Fig. S7 and S8, ESI†). Overall, these results clearly demonstrated the key factors influencing chirality induction from silica nanohelices to foldamers, including solvent evaporation rates (solvent nature and evaporation temperature) and the relative concentration of foldamers to silica helices, highlighting the crucial role of their interactions.

To further investigate the effect of foldamer-INHs interactions on chirality induction, silica nanohelices with three different surface types were used (Fig. 3(a)): (i) standard INHs, (ii) amine-functionalized INHs (referred to as INHs-NH_2), prepared by grafting (3-aminopropyl)triethoxysilane (APTES) onto the INHs surface, and (iii) calcinated-INHs, obtained by calcination of INHs at 600 °C for 2 hours under air. These INHs films were characterized by FT-IR (Fig. S9, ESI†). As shown in Fig. 3(b), (e) and Fig. S10 (ESI†), the ECD and CPL signals of Q_4 co-assembled with INHs-NH_2 film using the same protocol as above were significantly enhanced, with g_{abs} (324 nm) and g_{lum} (496 nm) values of approximately 3.7×10^{-3} and 3.6×10^{-3}, respectively. In contrast, *rac*-Q_4 on calcinated-INHs showed lower dissymmetry factors ($g_{abs} \sim \pm 5.1 \times 10^{-4}$ and $g_{lum} \sim \pm 6.6 \times 10^{-4}$). This trend was consistent for the longer *rac*-Q_6 and *rac*-Q_8 foldamers as well (Fig. S11, ESI†). The stronger chiral responses observed on the amine-functionalized silica compared to bare silica are likely due to enhanced hydrogen bonding interactions between the amine groups of silica surface and the aromatic groups of the foldamer helices. These interactions promote improved molecular organization. In contrast, thermal treatment of INHs at 600 °C, which reduces –OH groups, weakens the interaction between the silica helices and the foldamers.

We also evaluated the effect of foldamer length (*rac*-Q_n, n = 4, 6, 8 and 16) on the chiroptical signals. For all foldamers, symmetrical ECD and CPL spectra were measured demonstrating coherent ECD sign induction, with *rac*-Q_n/*P*-INHs and *rac*-Q_n/*M*-INHs exhibiting positive and negative ECD signals, respectively (Fig. 3(g), (h) and Fig. S12, S13, ESI†). Interestingly, the ECD signal intensity of *rac*-Q_n/INHs decreased as the foldamer length increased; specifically, the signal observed for *rac*-Q_4/INHs was 10 times higher than that of *rac*-Q_{16}/INHs. This result is in stark contrast to the previously observed trend for enantiomerically pure aromatic oligoamide helices.[26] In previous studies, the ECD response of helically locked foldamers with a chiral oxazolylaniline inducer at the N-terminal end exhibited a linear increase in intensity as their length increased up to 32 mer (Fig. 3(f)). These results were also in line with our findings with enantiopure aromatic oligoamide helices equipped with camphanyl inducer (Fig. S14, ESI†). The opposite trend observed with *rac*-Q_n/INHs suggests that longer oligomers require longer kinetics and higher deracemization energy, as previously demonstrated in solution by Huc *et al.*,[36] conditions that are not fulfilled when confined within the chiral nanospace.

Two possible explanations can be proposed for the chirality induction observed when *rac*-Q_n is drop-cast onto the INHs (Fig. 4(a)). The first explanation is that each foldamer enantiomer

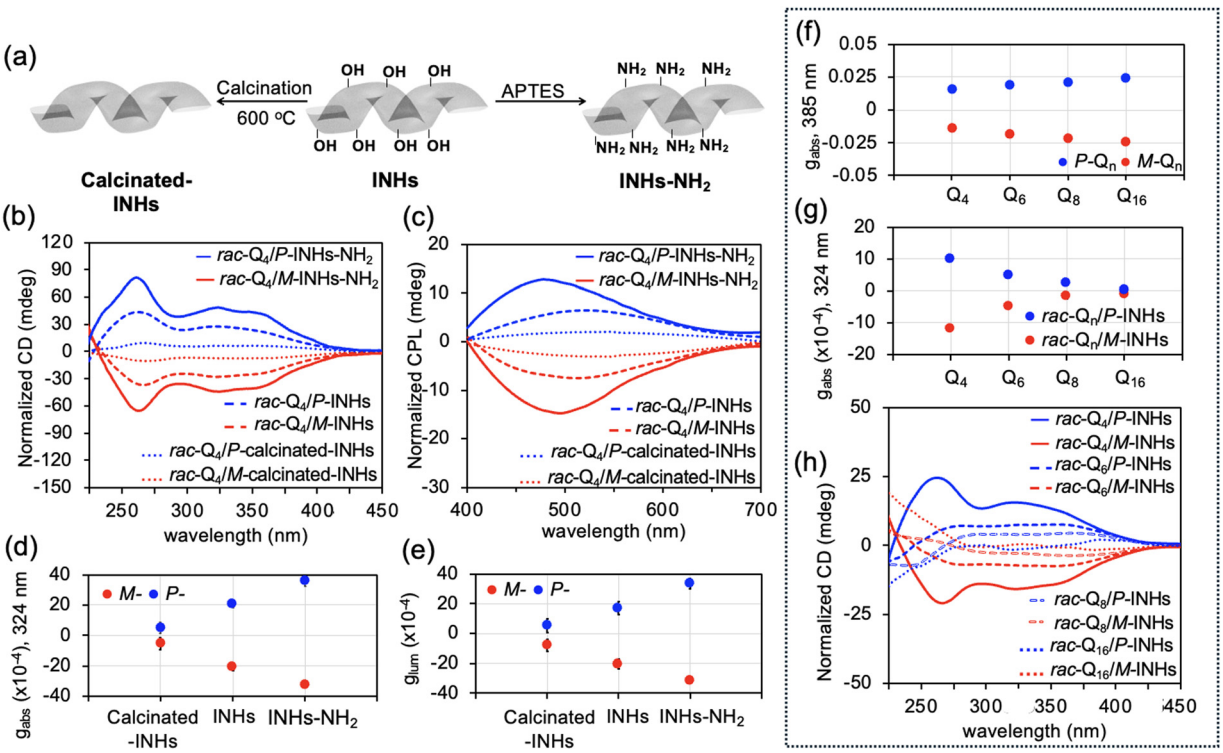

Fig. 3 (a) Three types of silica nanohelices including INHs, INH-NH_2 and calcinated INHs, (b) ECD-absorption spectra, (c) CPL spectra, (d) g_{abs} and (e) g_{lum} of *rac*-Q_4/INHs, *rac*-Q_4/INHs-NH_2, *rac*-Q_4/calcinated-INHs, (f) g_{abs} of *M*-Q_n/*P*-Q_n, (g) g_{abs} and (h) ECD spectra of *rac*-Q_n/INHs, respectively.

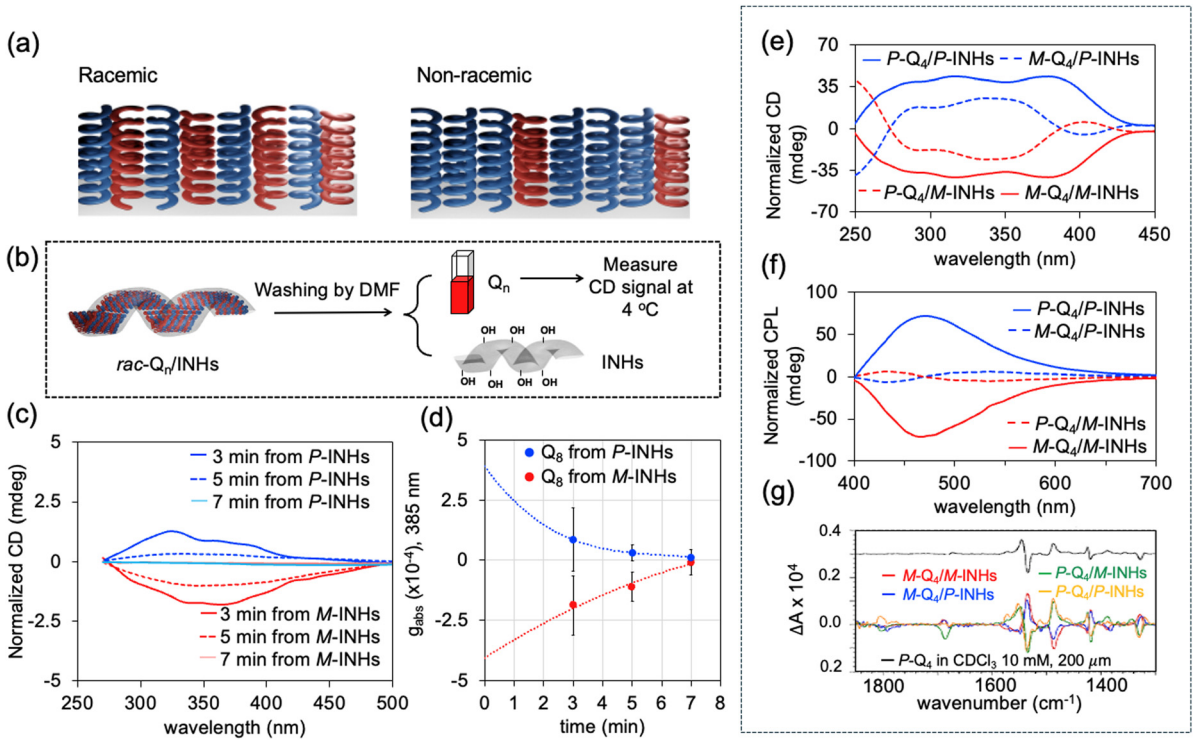

Fig. 4 (a) Illustration of the two possibilities after drop-casting *rac*-Q_n on INHs corresponding to the relation between g_{abs} and foldamers. (b) Recovering of Q_8 from INHs by simple washing with an organic solvent. (c) ECD spectra of *rac*-Q_8 in DMF after removing from INHs (average from 20-time experiment), (d) Plot between g_{abs} of *rac*-Q_8 (at 385 nm) in function of time with the standard deviation. (e) ECD-absorption, and (f) CPL spectra of *M*-Q_4/INHs and *P*-Q_4/INHs (λ_{ex} = 320 nm). (g) (top) VCD spectrum of *P*-Q_4 foldamer in $CDCl_3$ solution (10 mM, 200 μm pathlength). (bottom) Normalized differential VCD spectra of *M*-Q_4/*M*-INHs, *M*-Q_4/*P*-INHs, *P*-Q_4/*M*-INHs and *P*-Q_4/*P*-INHs samples after subtracting corresponding *rac*-Q_4/*P or M*-INHs.

has enantiospecific interactions with the silica nanohelices, resulting in enantiomeric enrichment (*i.e.* deracemisation). Alternatively, the foldamers could remain racemic but their intermolecular organization in the vicinity of the chiral nanospace of the INHs would be chiral.

To gain deeper insight into this question, *rac*-Q_8/INHs films prepared with toluene and dried were subsequently washed with DMF at 4 °C to separate Q_8 foldamers from the INHs (Fig. 4(b)). The ECD was measured immediately after the washing and separation from INHs to assess potential molecular chirality of Q_8 foldamers in solution in the absence of INHs. As length of the foldamer, *rac*-Q_8 was selected for this experiment as it offers an optimal balance between racemization kinetics (slower for longer foldamers) and the intensity of induced ECD signals (higher for shorter foldamers). This experiment at 4 °C was repeated 20 times for both *P*- and *M*-INHs, and the 20 ECD spectra were averaged (Fig. 4(c) and Fig. S15, ESI†). Consistent ECD signals were observed for the Q_8 wash solution, with signs corresponding to the INHs handedness. As expected for quinoline oligomer racemization in solution,[33] once removed from the INHs thin film, the ECD response of Q_8 rapidly decreased over time, reaching zero (fully racemized) within 7 minutes in all measurements.

The detection of such ECD signals for the Q_8 wash solution in the absence of INHs suggests an enantiomeric enrichment at the molecular level. By averaging the ECD signals at 3, 5, and 7 minutes, we estimated the enantiomeric excess (ee) at time zero (when Q_8 was still confined within the INHs). By comparing these ECD signals with those of enantiopure *P*- or *M*-Q_8, (with a camphanyl chiral inducer), the calculated enantiomeric excess (ee) values were approximately 4% for both *M*- and *P*-INHs (ESI†). Given the relatively low ee values, we conclude that the CD signals of *rac*-Q_n/INHs films primarily originate from the supramolecular assembly of the foldamer helices. This leads to the chiral organization of racemic foldamers in contact with the silica nanohelices, with only a minor contribution from molecular chirality due to the enantiomeric enrichment of the racemic foldamers.

To gain further insights into the contributions of molecular and supramolecular chirality, and to shed light on the different interaction between *P*- or *M*-INHs *vs.* *P*- or *M*-Q_n which co-exist in the racemic mixture of Q_n, we compared the ECD signals of the helically locked foldamer enantiomers *P*-Q_4 and *M*-Q_4 (Fig. 1(e)) in solution and in interaction with the INHs films (Fig. S16a and c, ESI†). In solution, *P*-Q_4 and *M*-Q_4 exhibit broad mirror-image CD signals between 300–400 nm, which can be attributed to the absorption of the quinoline backbones. The positive and negative signals at 385 nm correspond to the *P* and *M* handedness, respectively.[37] These foldamers also display CPL activity in the 400–700 nm range (λ_{ex} = 320 nm).[27] The CPL

signals of *M*-Q_4 and *P*-Q_4 molecules (Fig. S16b and d, ESI†) were similar to those observed from *rac*-Q_n/INHs (Fig. 1(i)), but with a notable blue shift (450 nm *vs.* 520 nm).

When *M*-Q_4 and *P*-Q_4 were drop-cast onto INHs thin films, with the foldamer and INHs having the matching helicities such as *M*-Q_4/*M*-INHs and *P*-Q_4/*P*-INHs, they exhibited strong mirror-image negative or positive ECD signals respectively throughout the 250–450 nm range. In contrast, with the mismatching helicities, such as *M*-Q_4/*P*-INHs and *P*-Q_4/*M*-INHs, they displayed weaker ECD signals (positive (negative) for *M*-Q_4/*P*-INHs (*P*-Q_4/*M*-INHs)) in the (270–350 nm range) with signal inversion observed around 380–420 nm (Fig. 4(e)). As discussed earlier, the chiroptical signals of the *rac*-Q_n/INHs hybrid systems primarily stem from the cooperative effect between the molecular chirality of the chiral foldamers and the supramolecular chirality induced by their interaction with the INHs. In the ECD signals, supramolecular chirality (negative for *M*-INHs and positive for *P*-INHs) dominates in the 275–375 nm range, while molecular chirality (also negative for *M*-Q_4 and positive for *P*-Q_4) prevails around 400 nm. This results in enhanced signals for *P*-Q_4/*P*-INHs and *M*-Q_4/*M*-INHs combinations across the investigated wavelength range, while signal attenuation and inversion are observed for *M*-Q_4/*P*-INHs and *P*-Q_4/M-INHs around 400 nm. This effect is more pronounced in the CPL signals (Fig. 4(f)), where *M*-Q_4/*M*-INHs and *P*-Q_4/*P*-INHs showed strong symmetrical CPL responses (negative and positive, respectively), while *M*-Q_4/*P*-INHs and *P*-Q_4/M-INHs displayed weaker CPL peaks with signal inversion at around 475 nm (negative/positive or positive/negative from short to long wavelengths). Negative CPL signals corresponded primarily to supramolecular chirality from *rac*-Q_n/*M*-INHs and molecular chirality of *M*-Q_4 with similar intensities, while positive signals were observed for *rac*-Q_n/*P*-INHs and *P*-Q_4. Due to the approximately 70 nm shift, signal cancellation was incomplete in mismatched combinations (*M*-Q_4/*P*-INHs and *P*-Q_4/*M*-INHs) was incomplete, resulting in signal sign inversions with significantly attenuated intensities instead.

Overall, chiral foldamers within an INHs environment with matching handedness (*M*-Q_4/*M*-INHs or *P*-Q_4/*P*-INHs) exhibited strong chiroptical properties. In contrast, chiral foldamers in INHs with mismatching handedness (*M*-Q_4/*P*-INHs and *P*-Q_4/*M*-INHs) displayed significantly lower ECD and CPL signals. The molecular chirality and intermolecular organizational chirality of the Q_4/INHs samples were also tracked using vibrational circular dichroism (VCD). INHs were deposited on CaF_2 windows, followed by drop-casting and drying *rac*-Q_4 or *rac*-Q_8 foldamers in toluene (5 mM) at 20 °C. VCD measurements were conducted at four different angles (0°, 45°, 90°, 135°), and averaged to minimize possible LD contributions. The raw VCD spectra of *rac*-Q_4/*M*-INHs samples display a pronounced positive-to-negative Cotton effect (from long to short wavenumbers) for the TO mode of the Si–O–Si asymmetric stretching vibration at around 1200–1000 cm^{-1}, while the opposite effect is seen for *rac*-Q_4/*P*-INHs samples (Fig. S17, ESI†).

In order to minimize the experimental artifacts from the optical setup and the strong silica contributions, baseline corrections were applied by subtracting the raw VCD spectra of silica helices from the raw VCD spectra of foldamers/silica helices, yielding differential (Q_n/*P*(*M*)-INHs − *P*(*M*)-INHs) VCD spectra. In Fig. S18 (ESI†), we compare the differential VCD spectra of racemic Q_4 *vs.* Q_8/INHs samples. In the spectra range 1750–1300 cm^{-1}, the signs of these differential VCD spectra are determined by the handedness of the INHs. Both *rac*-Q_4/*P*-INHs and *rac*-Q_8/*P*-INHs show positive VCD contributions across all the bands, whereas *rac*-Q_4/*M*-INHs and *rac*-Q_8/*M*-INHs exhibit negative VCD contributions, with relative intensities comparable to those in IR absorption measurements. The normalized VCD signals (with respect to the absorbance of the 1540 cm^{-1} band) of *rac*-Q_8/INHs are about half of those of *rac*-Q_4/INHs which is consistent with the ECD measurements. As demonstrated above, the dominant origin of chiroptical signal in these systems is supramolecular (with enantiomeric enrichment ~4%), the trend of weaker ECD and VCD signals for longer foldamers, even after normalization by monomer account, may be due to the poorer chiral supramolecular packing of longer foldamers on the silica nanoribbons due to the sterical hindrance. As shown and attributed in Fig. S19 (top) and Table S2 (ESI†), the IR spectrum of the *P*-Q_4/*M*-INHs sample provides vibrational information for the silica nanohelix, Q_4 foldamer, and camphanyl chiral inducer at different spectral ranges.

The normalized VCD spectra of racemic and enantiopure Q_4/*P*-IHNs are compared in Fig. S20 (ESI†), revealing weak but visible spectral differences between enantiopure and racemic Q_4 in the 1850–1300 cm^{-1} region. Again, these spectra confirm that the main contribution for the VCD signals come from the supramolecular chirality. To highlight the spectral differences between racemic and enantiomer (*P* or *M*) Q_4, in interaction with INHs, normalized differential VCD spectra of *rac*-Q_4/*P or M*-INHs samples were subtracted from the normalized differential VCD spectra of four types of enantiomers Q_4/INHs samples of the same handedness (Fig. 4(g), bottom), *i.e.* *M*-Q_4/*M*-INHs, *M*-Q_4/*P*-INHs, *P*-Q_4/*M*-INHs and *P*-Q_4/*P*-INHs. Four normalized differential VCD spectra were obtained, *i.e.* (*M*- or *P*-Q_4/*M*-INHs) – (*rac*-Q_4/*M*-INHs) or (*M*- or *P*-Q_4/*P*-INHs) – (*rac*-Q_4/*P*-INHs). They all show consistent patterns for molecular chirality induced by the camphanyl inducer (*R* or *S*). For example, the patterns of *P*-Q_4/*M*-INHs – *rac*-Q_4/*M*-INHs and *P*-Q_4/*P*-INHs – *rac*-Q_4/*P*-INHs (labelled *P*-Q_4/*M*-INHs or *P*-Q_4/*P*-INHs in Fig. 4(g)), match that of *P*-Q_4 free in $CDCl_3$ solution (Fig. 4(g), top), indicating that the VCD signals from inherent molecular chirality of enantiopure Q_4 foldamers and supramolecular chirality caused by their interaction with INHs can be thus differentiated.

Such observations reveal the complexity of interpreting raw VCD spectra for Q_4/INHs samples. Indeed, the VCD spectrum reported in Fig. S19 (ESI†) (bottom) combines the contributions of the silica nanoribbon chirality (1250–1000 cm^{-1}), the supramolecular chirality of enantiopure Q_4 in contact with silica, and the inherent molecular chirality of enantiopure Q_4 foldamers (1850–1300 cm^{-1}). Interestingly, while ECD and VCD both show additive effects between molecular and supramolecular chirality, their relative intensities of the two contributions are not the

same. Indeed, as shown in Fig. 4(e) and (f), the contributions of the molecular and supramolecular chiralities on the ECD and CPL spectra are of the same order of magnitude, whereas Fig. 4(g) and Fig. S20 (ESI†) reveal that the contribution of the supramolecular chirality is more pronounced than that of molecular chirality on the VCD spectra. The helical supramolecular organization of racemic or enantiopure foldamers (supramolecular chirality) is more effectively observed in VCD experiments. This is likely because the wavelength in the infrared region is significantly higher than the size of the silica nanohelices, making this technique more sensitive to the supramolecular contribution. This effect has already been mentioned in a previous article concerning the study of the molecular and supramolecular chirality in gemini-tartrate amphiphiles by ECD and VCD.[38]

4. Conclusions

The chiral interactions between aromatic oligoamide foldamers (Q_n) and mesoscopic silica nanohelices were systematically investigated. Racemic foldamers within the chiral environment of helical silica nanomaterials exhibited chiroptical properties, with g_{abs} and g_{lum} values around 1.0×10^{-3}. Key factors influencing the induction of chiroptical signals in *rac*-Q_n/IHNs films included drying temperature, solvent type, the *rac*-Q_n/IHNs ratio, the surface characteristics of the silica helices, and foldamer length.

The chiral memory transferred from the INHs to the foldamer helices remained detectable for a few minutes before complete racemization occurred after the foldamers were washed and separated from the INHs. This observation indicates that INHs induce enantiomeric enrichment of the foldamers. By analysing the relaxation profile of the CD signals and the intrinsic molecular CD properties of the foldamers, an enantiomeric excess (ee) of approximately 4% was extrapolated, attributed to the interaction between INHs and foldamers. Additionally, the interaction between enantiomeric foldamers with locked helicities and chiral INHs was explored. The ECD and CPL signals of chiral foldamers (*M* or *P*) were significantly influenced by the presence of INHs, resulting in either signal enhancement or attenuation, depending on whether the helicities of the foldamers and silica nanohelices matched or mismatched. This indicates that molecular chirality and supramolecular chirality arising from intermolecular helical organization work cooperatively, contributing hierarchically to the modulation of chiroptical ECD and VCD signals.

Overall, our results suggest that the primary source of chiroptical properties observed from *rac*-Q_n/INHs films is the spatial organization of foldamers within the chiral nanospace of the INHs, with a secondary contribution from the foldamer deracemisation (*i.e.* dynamic handedness inversion) in interaction with the helical silica. This work highlights the cooperative interactions where mesoscopic-level chirality from helical morphological materials interacts synergistically with molecular chirality.

Our findings introduce a new approach that leverages the enantiospecific interactions between small chiral molecules and mesoscopic helical silica nanostructures, highlighting the potential of these materials as promising platforms for enantioseparation and chiral catalysis.

Author contributions

P. P., Y. F. and R. O. conceptualized and designed the study. P. P., R. H., T. B., M. D. S. L. M., and C. O. performed the experiments and collected the data. A. B., Z. A., S. N., E. P., W. Y. and Y. F. analyzed the data and contributed to the interpretation of the results. E. M. provided technical support and instrumental expertise. Y. F. and R. O. supervised the project and wrote the manuscript with contributions from all authors. All authors reviewed and approved the final manuscript.

Data availability

The authors confirm that the data supporting the findings of this study are available within the article [and/or] its ESI.†

Conflicts of interest

The authors declare no competing financial interests.

Acknowledgements

This work was supported by CNRS, Université de Bordeaux, ANR-21-CE09-0012, Idex Bordeaux (Research Program GPR LIGHT), Grant-in-Aid for Scientific Research (JP23H01782), for Research Activity Start-up (24K23027), Core-to-Core program (JPJSCCA20250005) from Japan Society for the Promotion of Science (JSPS), and ''Start-up Research Grant 2024'' from TUMUG Support Program ''Promote Gender Equality and Female Researchers, Tohoku University''.

Notes and references

1 A. Garg, D. Rendina, H. Bendale, T. Akiyama and I. Ojima, Recent advances in catalytic asymmetric synthesis, *Front. Chem.*, 2024, **12**, 1–28.
2 M. E. Tiritan, M. Pinto and C. Fernandes, Enantioselective Synthesis, Enantiomeric Separations and Chiral Recognition, *Molecules*, 2020, **25**(7), 1713–1717.
3 A. Scalabre, A. M. Gutiérrez-Vílchez, Á. Sastre-Santos, F. Fernández-Lázaro, D. M. Bassani and R. Oda, Supramolecular Induction of Topological Chirality from Nanoscale Helical Silica Scaffolds to Achiral Molecular Chromophores, *J. Phys. Chem. C*, 2020, **124**, 23839–23843.
4 D. Yang, P. Duan, L. Zhang and M. Liu, Chirality and energy transfer amplified circularly polarized luminescence in composite nanohelix, *Nat. Commun.*, 2017, **8**, 15727.

5 K. Ding, J. Ai, Y. Duan, L. Han, Z. Qu and S. Che, Mechanism of diastereoisomer-induced chirality of BiOBr, *Chem. Sci.*, 2022, **13**, 2450–2455.
6 K. H. Park, J. Kwon, U. Jeong, J.-Y. Kim, N. A. Kotov and J. Yeom, Broad Chiroptical Activity from Ultraviolet to Short-Wave Infrared by Chirality Transfer from Molecular to Micrometer Scale, *ACS Nano*, 2021, **15**, 15229–15237.
7 H. E. Lee, H. Y. Ahn, J. Mun, Y. Y. Lee, M. Kim, N. H. Cho, K. Chang, W. S. Kim, J. Rho and K. T. Nam, Amino-acid- and peptide-directed synthesis of chiral plasmonic gold nanoparticles, *Nature*, 2018, **556**, 360–365.
8 P.-P. Wang, S.-J. Yu, A. O. Govorov and M. Ouyang, Cooperative expression of atomic chirality in inorganic nanostructures, *Nat. Commun.*, 2017, **8**, 14312.
9 S. Huo, P. Duan, T. Jiao, Q. Peng and M. Liu, Self-Assembled Luminescent Quantum Dots To Generate Full-Color and White Circularly Polarized Light, *Angew. Chem., Int. Ed.*, 2017, **56**, 12174–12178.
10 H. Kim, C. A. Figueroa Morales, S. Seong, Z. Hu and X. Gong, Perovskite-Supramolecular Co-Assembly for Chiral Optoelectronics, *ACS Appl. Mater. Interfaces*, 2024, **16**, 16515–16521.
11 K. Sugiyasu, S.-I. Tamaru, M. Takeuchi, D. Berthier, I. Huc, R. Oda and S. Shinkai, Double helical silica fibrils by sol–gel transcription of chiral aggregates of gemini surfactants, *Chem. Commun.*, 2002, 1212–1213.
12 T. Delclos, C. Aimé, E. Pouget, A. Brizard, I. Huc, M.-H. Delville and R. Oda, Individualized Silica Nanohelices and Nanotubes: Tuning Inorganic Nanostructures Using Lipidic Self-Assemblies, *Nano Lett.*, 2008, **8**, 1929–1935.
13 Y. Okazaki, J. Cheng, D. Dedovets, G. Kemper, M.-H. Delville, M.-C. Durrieu, H. Ihara, M. Takafuji, E. Pouget and R. Oda, Chiral Colloids: Homogeneous Suspension of Individualized SiO_2 Helical and Twisted Nanoribbons, *ACS Nano*, 2014, **8**, 6863–6872.
14 Y. Okazaki, T. Buffeteau, E. Siurdyban, D. Talaga, N. Ryu, R. Yagi, E. Pouget, M. Takafuji, H. Ihara and R. Oda, Direct Observation of Siloxane Chirality on Twisted and Helical Nanometric Amorphous Silica, *Nano Lett.*, 2016, **16**, 6411–6415.
15 Y. Okazaki, N. Ryu, T. Buffeteau, S. Pathan, S. Nagaoka, E. Pouget, S. Nlate, H. Ihara and R. Oda, Induced circular dichroism of monoatomic anions: silica-assisted the transfer of chiral environment from molecular assembled nanohelices to halide ions, *Chem. Commun.*, 2018, **54**, 10244–10247.
16 A. Scalabre, Y. Okazaki, B. Kuppan, T. Buffeteau, F. Caroleo, G. Magna, D. Monti, R. Paolesse, M. Stefanelli, S. Nlate, E. Pouget, H. Ihara, D. M. Bassani and R. Oda, Chirality induction to achiral molecules by silica-coated chiral molecular assemblies, *Chirality*, 2021, **33**, 494–505.
17 G. Duroux, L. Robin, P. Liu, E. Dols, M. D. S. L. Mendes, S. Buffière, E. Pardieu, A. Scalabre, T. Buffeteau, S. Nlate, R. Oda, M. S. Raju, M. Atzori, C. Train, G. L. J. A. Rikken, P. Rosa, E. A. Hillard and E. Pouget, Induced circular dichroism from helicoidal nano substrates to porphyrins: the role of chiral self-assembly, *Nanoscale*, 2023, **15**, 12095–12104.
18 N. Ryu, T. Kawaguchi, H. Yanagita, Y. Okazaki, T. Buffeteau, K. Yoshida, T. Shirosaki, S. Nagaoka, M. Takafuji, H. Ihara and R. Oda, Chirality induction on non-chiral dye-linked polysilsesquioxane in nanohelical structures, *Chem. Commun.*, 2020, **56**, 7241–7244.
19 J. Cheng, G. Le Saux, J. Gao, T. Buffeteau, Y. Battie, P. Barois, V. Ponsinet, M.-H. Delville, O. Ersen, E. Pouget and R. Oda, GoldHelix: Gold Nanoparticles Forming 3D Helical Superstructures with Controlled Morphology and Strong Chiroptical Property, *ACS Nano*, 2017, **11**, 3806–3818.
20 P. Pranee, A. Scalabre, C. Labrugere, N. Ryu, A. Yano, N. Hano, D. Talaga, Y. Okazaki, E. Pouget, S. Nlate, S. Bonhommeau, M. Takafuji, T. Wada, H. Ihara, T. Buffeteau, D. M. Bassani and R. Oda, Sequential chiral induction between organic and inorganic supramolecular helical assemblies for the *in situ* formation of chiral carbon dots, *Chem. Commun.*, 2023, **59**, 9762–9765.
21 P. Liu, Y. Battie, M. Decossas, S. Tan, E. Pouget, Y. Okazaki, T. Sagawa and R. Oda, Chirality induction to CdSe nanocrystals self-organized on silica nanohelices: Tuning chiroptical properties, *ACS Nano*, 2021, **15**, 16411–16421.
22 P. Liu, W. Chen, Y. Okazaki, Y. Battie, L. Brocard, M. Decossas, E. Pouget, P. Müller-Buschbaum, B. Kauffmann, S. Pathan, T. Sagawa and R. Oda, Optically Active Perovskite $CsPbBr_3$ Nanocrystals Helically Arranged on Inorganic Silica Nanohelices, *Nano Lett.*, 2020, **20**, 8453–8460.
23 P. Liu, Y. Battie, T. Kimura, Y. Okazaki, P. Pranee, H. Wang, E. Pouget, S. Nlate, T. Sagawa and R. Oda, Chiral Perovskite Nanocrystal Growth inside Helical Hollow Silica Nanoribbons, *Nano Lett.*, 2023, **23**, 3174–3180.
24 I. Huc, Aromatic Oligoamide Foldamers, *Eur. J. Org. Chem.*, 2004, 17–29.
25 A. M. Kendhale, L. Poniman, Z. Dong, K. Laxmi-Reddy, B. Kauffmann, Y. Ferrand and I. Huc, Absolute Control of Helical Handedness in Quinoline Oligoamides, *J. Org. Chem.*, 2011, **76**, 195–200.
26 D. Zheng, L. Zheng, C. Yu, Y. Zhan, Y. Wang and H. Jiang, Significant Enhancement of Circularly Polarized Luminescence Dissymmetry Factors in Quinoline Oligoamide Foldamers with Absolute Helicity, *Org. Lett.*, 2019, **21**, 2555–2559.
27 E. Merlet, K. Moreno, A. Tron, N. McClenaghan, B. Kauffmann, Y. Ferrand and C. Olivier, Aromatic oligoamide foldamers as versatile scaffolds for induced circularly polarized luminescence at adjustable wavelengths, *Chem. Commun.*, 2019, **55**, 9825–9828.
28 D. Bindl, E. Heinemann, P. K. Mandal and I. Huc, Quantitative helix handedness bias through a single H *vs.* CH_3 stereochemical differentiation, *Chem. Commun.*, 2021, **57**, 5662–5665.
29 Y. Ferrand, A. M. Kendhale, B. Kauffmann, A. Grélard, C. Marie, V. Blot, M. Pipelier, D. Dubreuil and I. Huc, Diastereoselective Encapsulation of Tartaric Acid by a Helical Aromatic Oligoamide, *J. Am. Chem. Soc.*, 2010, **132**, 7858–7859.
30 I. Huc and H. Jiang, *Supramolecular Chemistry:From molecules to Nanomaterials*, 2012, pp. 1–23.

31 C. M. Goodman, S. Choi, S. Shandler and W. F. DeGrado, Foldamers as versatile frameworks for the design and evolution of function, *Nat. Chem. Biol.*, 2007, **3**, 252–262.
32 X. Li, T. Qi, K. Srinivas, S. Massip, V. Maurizot and I. Huc, Synthesis and Multibromination of Nanosized Helical Aromatic Amide Foldamers *via* Segment-Doubling Condensation, *Org. Lett.*, 2016, **18**, 1044–1047.
33 H. Jiang, J.-M. Léger and I. Huc, Aromatic δ-Peptides, *J. Am. Chem. Soc.*, 2003, **125**, 3448–3449.
34 R. Oda, I. Huc, M. Schmutz, S. J. Candau and F. C. MacKintosh, Tuning bilayer twist using chiral counterions, *Nature*, 1999, **399**, 566–569.
35 T. Qi, V. Maurizot, H. Noguchi, T. Charoenraks, B. Kauffmann, M. Takafuji, H. Ihara and I. Huc, Solvent dependence of helix stability in aromatic oligoamide foldamers, *Chem. Commun.*, 2012, **48**, 6337–6339.
36 N. Delsuc, T. Kawanami, J. Lefeuvre, A. Shundo, H. Ihara, M. Takafuji and I. Huc, Kinetics of Helix-Handedness Inversion: Folding and Unfolding in Aromatic Amide Oligomers, *ChemPhysChem*, 2008, **9**, 1882–1890.
37 A. M. Kendhale, L. Poniman, Z. Dong, K. Laxmi-Reddy, B. Kauffmann, Y. Ferrand and I. Huc, Absolute Control of Helical Handedness in Quinoline Oligoamides, *J. Org. Chem.*, 2011, **76**, 195–200.
38 A. Brizard, D. Berthier, C. Aimé, T. Buffeteau, D. Cavagnat, L. Ducasse, I. Huc and R. Oda, Molecular and supramolecular chirality in gemini-tartrate amphiphiles studied by electronic and vibrational circular dichroisms, *Chirality*, 2009, **21**, E153–E162.

